Elaboration of oxide dispersion strengthened Fe-14Cr stainless steel by selective laser melting

E. Vasquez, P.-F. Giroux, F. Lomello, A. Chniouel, H. Maskrot, F. Schuster, P. Castany

HAL Id: hal-02043065
https://univ-rennes.hal.science/hal-02043065

Submitted on 7 Mar 2019

Elaboration of Oxide Dispersion Strengthened Fe-14Cr Stainless Steel by Selective Laser Melting

Authors:

Elodie Vasquez[a], Pierre-François Giroux[a], Fernando Lomello[b], Aziz Chniouel[b], Hicham Maskrot[b], Frédéric Schuster[c], Philippe Castany[d]

[a] DEN-Service de Recherches Métallurgiques Appliquées, CEA, Université Paris-Saclay, F-91191, Gif-sur-Yvette, France

[b] DEN-Service d'Etudes Analytiques et de Réactivité des Surfaces, CEA, Université Paris-Saclay, F-91191, Gif-sur-Yvette, France

[c] CEA Cross-Cutting Program on Materials and Processes Skills, 91191 Gif-sur-Yvette, France

[d] Univ Rennes, INSA Rennes, CNRS, ISCR – UMR 6226, F-35000 Rennes, France

Abstract:

This study presents the influence of the main selective laser melting (SLM) processing parameters on the densification behavior and microstructure evolution of oxide dispersion strengthened (ODS) Fe-14Cr stainless steel. Optimization of the process parameters allows to manufacture ODS stainless steel parts, which present high densities up to 98% and a fine dispersion of nanosized Y-Ti rich oxide particles. Laser power and scan speed are found to strongly influence the density and the microstructure of SLM builds. The ratio power over scan speed controls the width and the depth of the molten pool. Low energy densities (i.e. a low laser power or a high scan speed), inferior to 100 J.mm^{-3}, cause lack of fusion of the powder and induce the presence of numerous pores. Finer microstructure can be achieved in this condition since grains receive less energy to growth. The hatch distance does not affect the density in the range of testing values. A decrease in hatch distance causes re-fusion of previous neighbor track but does not re-melt the previous layer since the ratio power over speed is kept constant when varying the hatch distance. A slight coarsening of the microstructure is observed in this case. A large range of hatch distance can be used and especially large values, which decrease the time of production. This study can be a guideline to achieve materials with specific microstructure for high temperature applications.

[1]

Keywords:

Introduction:

Oxide dispersion strengthened (ODS) ferritic steels typically contain a fine dispersion of nanosized Y and Ti oxides, leading to an improvement in mechanical and physical properties, especially for high temperature applications (Wasilkowska et al., 2003). These alloys are being considered as a material for fuel cladding tubes in sodium fast breeder nuclear reactors, an application that requires a low swelling rate and high creep strength in a temperature range of 400-800°C (Šćepanović et al., 2016). ODS ferritic steels could also be used as combustion parts for engines, stirrers for the glass industry and other high temperature applications (A. R. Jones, 2010).

Conventional processing techniques, which involve melting such as foundry, tend to be avoided to produce ODS alloys since oxide particles can slag off into the molten pool which is detrimental for alloys creep strength. Therefore, ODS steels are usually produced by powder metallurgical process. Mechanical alloying (MA) consists firstly of milling **stainless** steel powder with oxides powders, leading to their dissolution into powder particles of steel. The powder is then consolidated by hot isostatic pressing or hot extrusion (Steckmeyer, 2012). This powder metallurgical process leads to high costs and limitations in terms of the final shapes of the consolidated materials. The evaluation and development of other alternative production methods, such as additive manufacturing, could thus increase the widespread use of ODS alloys.

Technological advancements in additive manufacturing techniques have recently shown promising results to produce ODS alloys (Arkhurst Barton Mensah, 2017; Boegelein et al., 2015). In this work, selective laser melting (SLM) is employed to consolidate a Fe14Cr1W + 0.3% Y_2O_3 + 0.3% TiH_2 powder, **produced by conventional route (Boutard et al., 2014).** The milled powder used as raw material is delivered as a thin layer onto a substrate. This layer is then melted by means of focused laser beam at each step. SLM process can produce dense solid freeform components which present high solidification cooling rates, allowing to retain a fine oxide dispersion without oxide particles coarsening in spite of several fusion steps.

[2]

Previous works focused on the evolution of the SLM process for consolidating PM2000 alloy, a FeCrAl ODS steel. Walker et al. (2009) demonstrated that a relative fine distribution of Y_2O_3 oxide particles with a mean particle size of 50 – 60 nm was retained in the built walls under certain processing parameters. Boegelein et al. (2015) studied further the microstructure and tensile properties of the built walls. They showed that it was possible, after a post-build anneal at 1200°C for 1 h, to get a room temperature strength similar to the one of conventional recrystallized PM2000. Hunt et al. (2015) used a similar process, selective laser sintering (SLS), to consolidate a Fe-base ODS-MA956 alloy. A density of 97% of wrought MA-956 alloy was achieved, as well as ultimate tensile strengths of only 65% of the wrought material strength. Since large pores and agglomeration of the yttria nano-particles were observed in the samples, thus leading to the loss of strength. Understanding the role of each SLM single processing parameter on the properties of ODS alloys is then essential to ensure the structural integrity of these alloys. In this work, the effects of laser power, scan speed and hatch distance on density, microstructure and precipitation are studied.

Materials and methods:

1. *Powder analysis*

A Fe-14Cr-1W-0.3Mn-0.3Si-0.2Ni **stainless** steel powder (supplied by Nanoval **and used as matrix material**) is milled with 0.3wt.% of Y_2O_3 oxide powder and 0.3wt.% of TiH_2 hydride powder during 176 hours under hydrogen atmosphere by Mecachrome on MATPERF Platform. **This step allows a homogeneous distribution of reinforcement in the matrix. The resulting powder is labelled powder M.** The integration of Y_2O_3 and TiH_2 compounds aims the formation of stable oxide particles such as $Y_2Ti_2O_7$ or Y_2TiO_5 in the stainless steel matrix (Miller et al., 2003 ; Zhang et al., 2016).

Figure 1 presents scanning electron microscope (SEM) images of the as-received **matrix** powder and the milled powder **M**. Before consolidation by SLM process, the powder **M** is sieved with a 80 μm mesh. This processing step allows the separation of the powder into a smaller average particle size (d_{50}) of 64 μm and a residual average particle size of 123 μm. **Powder M80 refers to the powder M after sieving.**

XRD patterns of (c) the matrix material and (d) the powder M

[3]

The nominal composition of the powder **M**, measured by an inductively coupled plasma optical emission spectrometry (ICP-OES), is displayed in table 1. The apparent density of the powder **M80** is measured as 3.8 g/cm^3 (48.8 % of the theoretical density). **XRD pattern of the powder M and powder M80 (Fig. 1c and 1d) show that only peaks corresponding to ferrite phase are visible since the content of reinforcement is very low to be detected by XRD measurements.**

2. Selective laser melting

Consolidations of powder **M80** are conducted on a TruPrint series 1000 SLM machine (TRUMPF GmbH), equipped with a 200 W Yb-fiber laser (λ=1.064 µm) and a spot size of 55 µm. The applied laser/scan range parameters are (Table 2): Laser power from 75 to **175** W, scan speed from 30 to 300 mm.s^{-1} and hatch distance from 50 to 250 µm. The powder bed feed rate is fixed to 50 µm per layer.

The consolidation process is performed under argon atmosphere in a sealed chamber. An argon gas injection ensures a constant flow in the build chamber with an imposed oxygen concentration lower than 100 ppm during the process. All samples consolidated by SLM process are cubes of 10 mm side (Figure 2a). Individual layers of these samples are scanned with parallel lines using bidirectional vectors separated by a specific hatch distance (HD). The scanning direction is altered by 90° between two consecutive layers, as shown in figure 2b.

The energy density (E) corresponds to the amount of applied energy per volume of material and it is defined by equation (1):

$$E = \frac{P}{V \times HD \times t} \tag{1}$$

where P is the laser power (W), V is the scan speed (mm.s^{-1}), HD is the hatch distance (mm) ant t is the layer thickness (mm) (Fayazfar et al., 2018).

3. Sample preparation and analytical techniques

The SLM builds are analyzed in the as-grown conditions. The density of each sample is measured thanks to Archimedes' method. The measures are repeated twice for each sample. Specimens are then prepared for SEM and Electron BackScattered Diffraction (EBSD) observations. Cross-sectional samples are polished by standard techniques with a final polishing step using a 40 nm colloidal silica suspension in order to reveal the microstructure. SEM and EBSD analyses are

[4]

conducted with a JEOL 7000F field emission gun (FEG) machine operating at 15 kV in backscattered electron (BSE) mode. Chemical analyses are performed by energy dispersive X-ray spectroscopy (EDS) on the same machine using a BRUKER EDS system.

The grain size is determined from analyzing cross-sectional optical micrographs of SLM builds viewed along the building direction. Etching to reveal the microstructure is performed on these samples, after prior 0.25 µm diamond polishing. The etchant is a solution consisting of 2.5 g of $CuCl_2$, 50 mL of hydrochloric acid and 50 mL of ethanol. The revealed grain morphology is studied using a Zeiss Axio Imager 2 optical microscope. More than 100 randomly chosen grains are measured in different areas of each SLM builds.

The micro-hardness is measured under a load of 9.8 N (1000 g) using a Vickers Struers Durascan device. Five lines containing 34 indentations are performed along the building direction and distributed in the whole width of samples. The micro-hardness is then averaged over the **170** indentations **and a confidence interval of 95% is given**.

Representative samples are observed by transmission electron microscopy (TEM). Sections of the SLM builds are then thinned from both sides to a thickness of about 100 µm. Discs with 3 mm in diameter are punched. Final thinning to electron transparency is performed thanks to an electropolishing system with a 10% perchloric acid in ethanol solution at a temperature of -10 °C. TEM imaging and EDS analyses are then conducted using a Jeol 2100 machine operating at 200 kV.

Results:

1. *Effect of SLM processing parameters on the density*

The final density of the SLM builds is compared to the final as-extruded bar density. This bar contains no porosity and has an absolute density of 7.751 g/cm^3. A first optimization of the processing parameters (laser power, scan speed and hatch distance) is performed to get a relative high density of the SLM builds. Based on this data, two processing parameters are fixed and the third one is modified in order to study the effect of each parameter on the final density.

Laser power is studied in the range from 75 to **175** W. Figure 3a presents the evolution of relative density as a function of laser power. The relative density increases when the laser power increases. For values of laser power higher than **150** - **175** W, the relative density **begins to remain**

[5]

nearly constant at 98%. **The maximum laser power reached by the machine used in this study is limited to 175 W. Results show that higher laser power values should lead to produce fully dense SLM builds.** Hatch distance is varied from 50 to 250 µm. As shown in figure 3b, the relative density remains constant with the evolution of hatch distance. HD has no influence on the density with the set of other used parameters. Scan speed is studied in the range from 30 to 300 mm.s^{-1}. The evolution of the relative density as a function of scan speed is given in figure 3c. This plot shows that the relative density reduces as the scan speed increases. As observed for the laser power, it seems that for values of scan speed lower than 100 mm.s^{-1}, the relative density remains stable at 98%.

Figure 4 shows the distribution of porosities as a function of various processing parameters. It can be seen that a decrease in laser power as well as an increase in scan speed induce the formation of many porosities (Figure 4c,d,e,f). These porosities are oriented mostly along the building direction. The most porous samples are obtained with an energy density lower than 100 J.mm^{-3}. These porosities could be attributed to a lack of fusion (Tang et al., 2017). Porosities observed in SLM samples build at various hatch distance are mostly oriented horizontally (Figure 4i,j,k,l).

Several scanning strategies are explored to elaborate SLM builds as illustrated on figure 2. Using an island scanning strategy is often preferred to scan large parts because that decreases residual stresses and distortion (Gibson et al., 2015). However, it can be seen in this study that some defects such as porosities are specially localized in the regions between different islands, as shown in figure 5a (red arrows). This phenomenon can be minimized by decreasing the hatch distance (Figure 5b). The smaller the overlaps between islands are, the higher is the number of porosities observed between the various islands. The non-spherical shape of the powder can promote this phenomenon. It is also observed a decrease in terms of density by rotating the island scanning pattern of 45° rather than 90°. When the rotation angle decreases, the number of miss-overlap could increase and at the same time could increase the porosity formation. In this study, a simple scanning strategy with parallel lines is then used since the influence on the main processing parameters (P$_{laser}$, V$_{scan}$, H.D.) is on focus. Moreover, this simple scanning strategy produces parts with better densities than those elaborated with an island scanning strategy.

[6]

2. *Effect of SLM processing parameters on the microstructure*

As shown in figure 6, a microstructure with columnar grains oriented along the SLM growth direction is observed on all the SLM builds. A small number of build defects such as small pores is observed, especially for the samples built at high scan speed or at low laser power. These pores have irregular shape ascribed to the lack of liquid metal to fully complete the area drawn by the laser (Bai et al., 2017). This kind of microstructure is significantly different that those observed in conventional ODS alloys (García-Junceda et al., 2012).

Table 3 displays the grain's size of SLM builds at different processing parameters. **Grains are longer than the molten pool's depth that means they extend into at least the 5 previous layers. The higher the laser power, the longer the grains.** The sample built at 100 W shows a microstructure finer than the sample built at **175** W (**27** vs. **31** μm for width and **226** vs. **495** μm for length). Laser power influences thus the microstructure by affecting the grain size**, especially the length**: Lower is the laser power and smaller are the grains. Similar conclusions can be made for the influence of hatch distance and scan speed on the microstructure. However, the impacts of these both parameters on the microstructure are less significant than the impact of laser power on the grain size. These observations show that (i) higher is the scan speed and smaller are the grains and (ii) higher is the hatch distance and smaller are the grains. The grain size measured in the sample built at 175 W, 300 mm.s^{-1} and 195 μm is strongly influenced by numerous porosities observed on the sample. Indeed, the presence of pores in the microstructure impedes the grain growth and thus decreases the measured grain size.

3. *Effect of SLM processing parameters on the texture*

EBSD is performed on as-SLM built samples to analyze the texture. The choice of processing parameters strongly influences the texture, as shown in figure 7, which shows pole figures of as-grown SLM built samples for various processing parameters. The analyses reveal a strong <001> texture along the growth z-direction **for the sample built at 175 W, 100 mm.s^{-1} and 195 μm (Fig. 7a).** . ⟨001⟩ directions are known to be the easy-growth directions for body centered cubic metals (Kou, 2002). A decrease in laser power induces a decrease of the ⟨001⟩ texture along the building direction (Fig. 7c). When a low scan speed (30 mm.s^{-1}) is used, the texture changes from ⟨001⟩ to mainly ⟨111⟩ directions along the growth direction (Fig. 7d). This change in texture is ascribed to a modification of the melt

[7]

pool's shape. **The ratio power over speed determines the width and the depth of the molten pool. That is why both parameters strongly influence the texture of the SLM builds.** In contrary to the laser power and the scan speed, the hatch distance has no influence on the texture (Fig. 7a and 7b). **A modification of the hatch distance does not affect the shape of the molten pool and, in turn, does not have a significant impact on the texture.**

4. *Effect of SLM processing parameters on the microhardness*

Table **3** displays the microhardness of SLM builds at various processing parameters **and the microhardness of an extruded ODS stainless steel (García-Junceda et al., 2012).** The sample built **at 175 W, 100 mm.s^{-1} and 195 µm** shows the highest microhardness value of 189 HV. A **decrease in** laser power or **an increase in** scan speed **cause a loss of** hardness **and density**. **The effects of laser power and scan speed on the mircohardness will be discussed further in the last section.** . A hardness of 173 HV is obtained for the sample built at 175 W, 100 mm.s^{-1} and with a hatch distance of 50 µm while a hardness of 189 HV is obtained with the same laser power, the same scan speed but a hatch distance of 195 µm. Both samples have also similar densities. This shows that a decrease of hatch distance induces a decrease of hardness.

The hardness of ODS stainless steels manufactured by SLM process is lower than the hardness measured on conventional ODS stainless steels. This result can be explained by the significant difference in grain size obtained after both processes (~ 30 µm vs. ~ 2 µm for the width and ~ 370 µm vs. ~ 6 µm for the length).

5. *Description of the nanometric precipitation inside SLM builds*

The presence of a fine dispersion of oxyde particles inside the SLM builds is studied using SEM and TEM techniques. In spite of several fusion steps, which occur during the SLM process, it can be possible to retain a fine dispersion of precipitates inside the SLM parts without agglomeration of those.

Two size ranges of precipitates are observed: precipitates with a mean diameter around 60 nm on SEM images (Figure 8a) and precipitates smaller than 10 nm on TEM images (**Figures 8b and 8c**). Similar results were obtained by Boegelein et al. (2016). These precipitates are rich in oxygen,

[8]

titanium and yttrium according to the EDX analysis. They are homogenously dispersed inside grains of each SLM builds. Very few particles are observed on grain boundaries (Figure 8a).

Some precipitates are studied more precisely to identify the oxide types formed during the SLM process (Figure 9). According to the EDX results, the precipitate numbered 1 has a high content of Y, Ti and O elements. Atomic proportions of these different elements show a Y/Ti ratio of 0.93. Average inter-reticular distances of 0.585 nm and 0.186 nm are found on the corresponding diffraction pattern. This is coherent with the inter-reticular distance of 0.582 nm for the {111} planes of $Y_2Ti_2O_7$ and with the inter-reticular distance of 0.1784 nm for the {044} planes of $Y_2Ti_2O_7$, which has a cubic pyrochlore structure. Diffraction pattern coming from this oxide reveals spots with lower intensity, which are typical of surstructure spots of such pyrochlore structure (Badjeck et al., 2015). On the same image, the precipitate numbered 2 is also rich in elements of Y, Ti and O. The atomic Y/Ti ratio is around 0.76. Average inter-reticular distances of 0.367 nm and 0.236 nm are measured on the corresponding diffraction pattern. This might be consistent with the inter-reticular distance of 0.351 nm coming from the {210} planes belonging to YTi_2O_6 oxide, which has an orthorhombic symmetry. The inter-reticular distance of 0.236 nm is exactly the expected inter-reticular distance for the {112} planes of YTi_2O_6 oxide. $Y_2Ti_2O_7$ is classically observed in conventional ODS alloys (Zhang et al., 2016) and YTi_2O_6 is another possible stable Y-Ti-O oxide (Dumont et al., 2014).

Discussion:

1. *Role of processing parameters on density of SLM builds*

The influence of laser power and scan speed on the final relative density is significant by the range of analysis. Theoretically, by increasing the laser power as well as by decreasing the scan speed allow to fully melt the powder. **In this case, refusion occurs in-depth.** Bai et al. (2017) studied the influence of processing parameters during the elaboration of maraging steel 300 by selective laser melting. In their study, they explained that when the laser power is higher than a specific value, vaporization and spatter occur and induce a lack of liquid metal to fill the molten track leading to the formation of voids. **AlMangour et al. (2018) studied the influence of the energy density (by changing the scan speed) on the densification behavior of TiC/316L stainless steel nanocomposites elaborated by SLM. They found that samples made with the lowest energy density (67 J.mm^{-3}), which means at the highest scan speed, presents large pores, which could**

[9]

be attributed to balling defects coming from liquid instability due to Marangoni convection. On the contrary, sample built at the highest energy density (300 67 J.mm^{-3}), which means at the lowest scan speed, presents a density of 98.2%. Only few pores and thermal cracking are visible due to high operating temperature and low viscosity of the metal liquid, which promotes the backfilling of shrinkage voids.

In our present study, the powder used is coarser than the powder used by Bai et al. **and Almangour et al.** (30 - 110 µm, **30 – 56 µm** and 15 – 45 µm respectively). Therefore, it is necessary to provide higher energy to fully melt the powder. This phenomenon explains the increase in relative density with the increase in laser power and the decrease of scan speed. **Regarding figure 4, it is necessary to use at least 100 67 J.mm^{-3} to get between 97 and 98% of density for the SLM builds.** It could be assumed that for laser power **much** higher than 175 W or for scan speed lower than 30 mm.s^{-1}, the relative density would decrease because of the keyhole-mode effect. As described by King et al. (2014), the keyhole-mode laser melting resulted in melt pool deeper than those observed in a conduction mode. If the melt pool reaches a high enough temperature, vaporization of metal takes place. The molten material will push out and a cavity will form if the pressure of theses vapors exceeds the surface tension.

Complete densification is not achieved in the range of tested processing parameters in this study. It might be due to the available maximum laser power, which is not high enough to allow the complete melting of the powder layer in order to avoid lack of fusion porosities. However, a too high energy input could also cause evaporation of metal liquid leading to the formation of fine spherical pores (attributed to trapped gas) and thermal cracks, as explained by AlMangour et al. (2018). To avoid this phenomenon, Attar et al. (2014), which studied the elaboration by SLM of in situ titanium - titanium boride composites, showed that when both laser power and scan speed increased at a constant energy density (enough to melt the powder layer), the keyhole effect was decreased and the relative density was increased. In the present study, a simultaneously increase in laser power and scan speed at constant energy density could result in builds with higher densities.

When the hatch distance decreases, the overlap between two tracks increases. The latter induces an increase of the energy transferred to the material on a limited area that allows to fully melt

[10]

the powder. **Attar et al. (2018) explained that an increase in hatch distance induces a decrease in density and a refinement of the microstructure when titanium-based matrix composites are elaborated by SLM.** However, **in the present study**, no significant variation in density is observed when the hatch distance is varied from 50 to 250 µm, as shown in figure 3b. **Porosities mostly oriented horizontally are visible on figure 4i,j,k,l. It might be assumed that the re-melting takes place laterally and not in depth when the hatch distance decreases. Samples built at various hatch distances are produced with an energy density higher than 140 67 J.mm^{-3}, which is high enough to avoid formation of lack-of-fusion porosities. Samples built with the lowest hatch distance (100 and 50 µm) present the most elongated pores in horizontal direction (Figure 4k,l). This kind of pores could result from thermal cracks since these samples are made at elevated energy densities (350 and 700 67 J.mm^{-3} respectively). Keyhole mode thus occurs and impedes a complete densification, as suggested by Almangour et al. (2018).**

Some experiments were carried out to estimate the track's width. Single straight tracks are consolidated through a laser power of **175** W and a scan speed of 100 mm.s^{-1}. The mean width of theses tracks is around 215 µm. **Some melt pools are also visible on optical images from etched specimen side views. The width could be estimated between 250 and 300 µm and the depth are around 60 – 70 µm for the sample built at 175 W, 100 mm.s^{-1} and with a hatch distance of 195 µm.** It could be expected the existence of a threshold value of hatch distance, above which voids are left between two tracks and degrade the density. This value is not reached in the present study.

A hatch distance of 50 µm represents an overlap of 77%. In such processing conditions, the metal is exposed to almost complete re-melting. Yasa and Kruth (2011) showed that a 316L stainless steel part exposed to laser re-melting exhibited an increase in density and a decrease in surface roughness. **This phenomenon could explain that high applied energy density does not affect significantly the density.**

Finally, in the present study, a large range of hatch distance can be used without significant impact on the density of SLM builds, which gives good reproducibility and productivity to this process. **The hatch distance has to be chosen in accordance with the ratio power over scan speed, which determine the track's width and depth.**

[11]

2. Role of processing parameters on the grain structure

The grain structure of SLM builds depends on the melting and solidification of the molten pool. There are two classical kinds of shape for the molten pool: It can be semicircular or keyhole in cross section depending on the heat intensity transfers into the material during the process (DebRoy et al., 2018). The shape of the molten pool during SLM process has usually a high length to depth ratio (Kou, 2002). In this case, the grains will be oriented along the building direction in order to grow perpendicular to the pool boundary. As observed here, this favored growth direction will conduct to a majority of columnar grains along the building direction (Figure **6**).

The thermal history during the SLM process has also a strong influence on the grain size and orientation. Rapid heating, fast solidification and re-melting of the previous and adjacent layers strongly affect the formation of grains. All these phenomena are driven by the processing parameters, which can be related to the energy density. For example, an increase in laser power input P will increase the energy density. The heat flow becomes more important inside the material, which induces the formation of deep molten pool and therefore more reheating of the previous layer. **This phenomenon promotes an epitaxial growth of grains between each layer and promotes the texture along the ⟨001⟩ directions (AlMangour et al., 2017). This explains the decrease in texture observed with lower laser power (100 vs. 175 W), since refusion occurs in lower depth (Figure 7).**

Our observations also show a change in texture when the scan speed is low (30 mm.s^{-1}). At this low scan speed, the molten pool changes from a tear-drop shape to a more circular shape as it can be observed on the top view of tracks by optical microscope. In this condition, the molten pool becomes similar to those observed in direct energy deposition (DED) process. As explained by DebRoy et al. (2018), in DED process, melt pools have similar depth and length. The molten pool is more curved and therefore induces the growth of longer and more curved columnar grains **perpendicularly to the molten pool boundary**. **At this low scan speed, the cooling rates are strongly reduced. Grains have more time to grow** preferentially along the densest ⟨111⟩ directions of the bcc structure **rather than along the energetically favorable ⟨001⟩ directions**.

The cooling rate has also a significant influence on the grain size. Finer grain structure is obtained from higher cooling rates because grains have less time to grow (DebRoy et al., 2018). In the

[12]

present study, a coarsening of grains is observed when the energy input increases and thus when the cooling rate decreases, i.e. when the laser power increases and when the scan speed and hatch distance decrease. Concomitantly, as the highest gradient temperature is in the growth direction, a $\langle 001 \rangle$ texture is promoted along the building direction (Herzog et al., 2016).

In the present study, the hatch distance affects only the grain size but not the texture of the SLM builds. If the ratio power over scan speed is kept constant, the width and the depth of the molten pool do not change with the variation of the hatch distance. That is why no change in texture is observed by varying the hatch distance from 50 to 195 μm. When a small hatch distance is chosen (50 vs. 195 μm), more reheating of the adjacent layers occurs. This affects the cooling rates and potentially affect the grain growth. This phenomenon explains the coarsening of the microstructure when the hatch distance decreases.

Process parameters optimization is essential to control the microstructure rather than the control of density is **also** provided by a good control of the powder. In the current study, powder particles are characterized by a non-spherical shape, which could impact the powder bed density. Voids might left during the spread of powder and promote the formation of porosities. Boisselier and Sankaré (2012) showed that the morphology of the powder affects the laser/powder interaction, while Liu et al. (2011) found that powder with higher powder bed density generates parts with higher density. Investigations are currently in progress in order to better understand the influences of powder characteristics on SLM builds.

3.   *Microstructure comparison between ODS* **stainless** *steel parts made by conventional route and SLM process*

The grain morphology of Fe-14Cr ODS steels fabricated by a conventional route were studied extensively, e.g. by Garcia-Junceda et al. (2012). They studied the influence of the microstructure on the tensile and impact strength properties of an extruded and annealed Fe-14Cr-1W-0.4Ti-0.3Y_2O_3 ODS alloy bar. Two kinds of grains are distinguished: Some small grains with an anisotropic texture accompanied by a majority of long grains elongated along the extrusion direction with a preferential $\langle 110 \rangle$ direction. Typically, the average size of smallest grains and the mean length of elongated grains are about 0.7 μm and 4.9 μm, respectively. In the present study, grain size obtained by SLM process have a mean length of about 400-500 μm as a function of processing parameters.

SLM process induces high temperature gradient and high solidification velocity of the melt pool, which lead to columnar grain morphology along the building direction (DebRoy et al., 2018). In the present study, the layer thickness of the powder-bed was fixed to 50 µm and grains are much longer than 50 µm. It means that the depth of melt pool does not limit the growth of grains. The re-melting of the previous layer allows the grains to grow through the various layers. In addition, this re-melting leads to promote grains coarsening, which can explain the large grain size.

Compared to a conventional route, extrusion followed by an annealing does not induce such coarsening of grains, since the melting temperature of the metal is not reached. This observation conflicts with the refinement in microstructure classically observed for additively manufactured parts in comparison with cast samples (Herzog et al., 2016). For example, Song et al. studied the microstructure and the mechanical properties of 316L stainless steel manufactured by SLM process (2014). They showed that the fine-grained microstructure and the higher dislocations density leads to improve the mechanical properties. Since conventional processing techniques used for ODS steels are different from casting method and SLM process, it would be better to compare the microstructure of ODS SLM parts to those obtained by welding process. Indeed, SLM presents many similarities with welding: a moving heat source and a fusion zone in displacement with the heat source (DebRoy et al., 2018). However, fusion joining techniques are generally unsuccessful to produce ODS steels since melting induces agglomeration of precipitates.

Friction stir welding is usually preferred to join ODS steels: This process induces a local temperature close to the melting point without reach it. Dawson et al. studied the microstructure of ODS steels produced by friction stir welding (2017). They obtained grains with an aspect ratio of about 2 and a mean diameter between 2 and 3 µm, which is close to the conventional microstructure. They also observed a decrease in the measured volume fraction of nano-particles dispersion in the welds as compared to the base material. The additive manufacturing process seems to be the only process, which allow to produce ODS steels despite several melting steps. Thanks to the SLM process, it is possible to elaborate new microstructure for ODS stainless steels. The microstructural characteristics can be controlled thanks to a precise selection of the processing parameters.

[14]

4. Role of SLM processing parameters on the microhardness

Several parameters can influence the hardness: the grain size based on the Hall-Petch's law, the internal stresses, the initial density of dislocations and the density of precipitates (Praud et al., 2012). The initial density of dislocations and the density of precipitates were not measured in the present study. Generally, an increase in relative density of the material leads to an increase in hardness measurements for additive manufacturing parts, as analyzed by J. Zuback and T. Debroy (2018). However, a variation in relative density is often correlated with a change in processing parameters, inducing modification of the cooling rates and the molten pool geometry, which affect the microstructure, the internal stresses values and thus the hardness. Thijs et al. (2010) showed a correlation between the microhardness and the applied energy density but not with the density of the samples. Their results highlighted that a higher energy density, applied by decreasing the scanning speed or the hatch distance, induces an increase in microhardness.

In the present study, a decrease in laser power (lower than 175 W) or an increase in scan speed (higher than 100 mm.s^{-1}) induces a loss of density, as shown in figure 3a and 3c and induces the formation of smaller grains, as shown in table 3. The refinement in microstructure should increase the microhardness as described by the Hall-Petch law (Petch, 1953). **However, this refinement is mainly observed on the length of the grains but not on their width. This refinement does not impact the microhardness since the size of a print after load is around 100 µm, which is smaller than the length of the grains. The microhardness values across the building direction are similar to those along the building direction for the both samples manufactured at 100 W; 100 mm.s^{-1}; 195 µm and at 175 W; 300 mm.s^{-1}; 195 µm. A change in processing parameters could also affect the internal stresses and thus the microhardness.**

A decrease in hatch distance from 195 to 50 µm **induces a loss of microhardness of 16 HV.** A decrease in hatch distance also induces a coarsening of the microstructure**, mainly for the width of the grains**. In this case, the coarsening of the microstructure could be responsible for the loss of micro-hardness. **These results are in accordance with the work of Yang et al. (2017), in which TiAl/TiB$_2$ metal matrix composites were processed by SLM by varying the hatch distance. An**

[15]

increase in nanohardness was observed when the scan line spacing increased thanks to the refinement of the microstructure and the increase of TiB_2 content.

A decrease in microhardness is also observed when the analysis are performed across the building direction rather than along the building direction for the samples manufactured at 175 W, 100 mm.s^{-1}and 195 μm or 50 μm. These losses in hardness cannot be explained by an effect of the grains size. Typically, grains are finer across the building direction what should increases the microhardness (Praud et al., 2012), but this phenomenon is not observed on the studied material.

The Hall- Petch's law described the effect of grains size (d) on the induced stress (σ) following the equation (2):

$$\sigma = \frac{k}{\sqrt{d}} \tag{2}$$

with k a constant. The induced stress decreases with the grain size, which decreases the hardness. Finally, the difference in grains size between all the samples processed by SLM are probably not significant enough to affect the microhardness. Internal stresses could affect significantly the measured values of the microhardness. Indeed, heat treatments were performed on ODS stainless steels manufactured by SLM process and microhardness measurements on these samples, and results show a loss of around 30/40 HV without change in grain sizes. This evolution of microhardness values comes probably from a release of internal stresses thanks to the heat treatment.

The hardness of ODS steel processed by SLM is similar to the values measured in wrought steels, which are between 120 and 200 HV (Charles et al., 2009; Dongsheng et al., 2016). As wrought steels have finer microstructure than ODS steel elaborated by SLM process, the gain in hardness due to the addition of reinforcement might hide by the coarsening of the microstructure.

The change in density of precipitates by a change of processing parameters could also affect the micro-hardness. Prashanth et al. (2016) showed that the addition of TNM reinforcement in the Al-12Si matrix leads to an increase in microhardness mainly due to the apparition of Al_6MoTi intermetallic phase harder than the matrix (3.95 GPa vs. 1.62 GPa). In the present study, no phase transformation is observed. The effect of reinforcement on the microhardness might

[16]

thus be less effective. This phenomenom is not investigated in the present study. **The powder might be also optimized by changing the content of reinforcement for the SLM elaboration.**

5. *Comparison between the precipitation in ODS* **stainless** *steel made by conventional route and SLM process*

Conventional ODS stainless steels are characterized by a homogeneous distribution of nanosized oxide Y-Ti-O precipitates. Garcia-Junceda et al. (2012) observed particles inside ferritic grains. These are Y-Ti-O oxides and Y-Ti-Al-Si-O particles, both with size ranging between 2 and 50 nm. Large particles from 60 to 240 nm are also observed and are located preferentially at grains boundaries. These particles are identified as Ti-Al oxides. Some bigger Ti-Al particles (from 300 to 650 nm) are also identified as nitrides. The size of Y-Ti-O precipitates is usually lower than 10 nm (Zhao et al. 2017). On the contrary, all the observed precipitates in SLM builds are composed by yttrium, titanium and oxygen elements, regardless of their size. No carbides, titanium or aluminum oxides are observed. No agglomerations of particles or significant variation in precipitates density between different grains or along grain boundaries are observed.

In conventional ODS alloys, Sakasegawa et al. (2009) showed a correlation between the size of oxide precipitates and their chemical composition. Precipitates with diameter lower than 15 nm are non-stoichiometric $Y_xTi_yO_z$ oxides. From 15 to 35 nm, oxide particles are identified as $Y_2Ti_2O_7$ pyrochlore oxides. Finally, precipitates larger than 35 nm are TiO_2 particles with a low yttrium content. In SLM builds of the present study, $Y_2Ti_2O_7$ oxides larger than 35 nm are observed, as shown in figure 8. Moreover, both oxides observed in figure 8 have almost the same size but significant variation of their chemical composition are measured. Results of the observations performed on all the ODS **stainless** steel samples built by SLM show that all oxides formed during SLM process are mainly composed by yttrium, titanium and oxygen, regardless of their size.

Conclusion:

In this work, the manufacture of ODS Fe14Cr alloys by SLM process is studied and provides the development of innovative microstructure. The effects of the SLM process parameters on density and microstructure are investigated and the following conclusions can be drawn:

- Samples with high density (> 98 %) and fine dispersion of nanosized Y-Ti-O particles are obtained with optimized processing parameters.

[17]

- The density increases with high laser power and low scan speed. Hatch distance does not affect significantly the density of the samples since this parameter is selected in a size range close to the track's width**, which is determined by the ratio power over scan speed.**

- The parts manufactured by SLM has columnar grains along the building direction with a microstructure significantly different than those usually observed in conventional ODS alloys.

- The processing parameters have a significant influence on the grain size. High laser power, low scan speed and low hatch distance conduct to a coarsening of the microstructure.

- Only Y-Ti-O oxides are observed in SLM builds with a chemical composition not impacted by their sizes. These precipitates are homogeneously distributed inside the grains without any agglomeration.

References:

A. R. Jones, 2010. Historical perspective: ODS alloy development.

AlMangour, B., Grzesiak, D., Borkar, T., Yang, J.-M., 2018. Densification behavior, microstructural evolution, and mechanical properties of TiC/316L stainless steel nanocomposites fabricated by selective laser melting. Materials & Design 138, 119–128. https://doi.org/10.1016/j.matdes.2017.10.039

AlMangour, B., Grzesiak, D., Yang, J.-M., 2017. Scanning strategies for texture and anisotropy tailoring during selective laser melting of TiC/316L stainless steel nanocomposites. Journal of Alloys and Compounds 728, 424–435. https://doi.org/10.1016/j.jallcom.2017.08.022

Arkhurst Barton Mensah, Park Jin-Ju, Lee Chang-Hoon, Kim Jeoung Han, 2017. Direct Laser Deposition of 14Cr Oxide Dispersion Strengthened Steel Powders Using Y2O3 and HfO2 Dispersoids. Korean J. Met. Mater. 55, 550–558. https://doi.org/10.3365/KJMM.2017.55.8.550

Attar, H., Bönisch, M., Calin, M., Zhang, L.-C., Scudino, S., Eckert, J., 2014. Selective laser melting of in situ titanium–titanium boride composites: Processing, microstructure and mechanical properties. Acta Materialia 76, 13–22. https://doi.org/10.1016/j.actamat.2014.05.022

Attar, H., Ehtemam-Haghighi, S., Kent, D., Dargusch, M.S., 2018. Recent developments and opportunities in additive manufacturing of titanium-based matrix composites: A review. International Journal of Machine Tools and Manufacture 133, 85–102. https://doi.org/10.1016/j.ijmachtools.2018.06.003

Badjeck, V., Walls, M.G., Chaffron, L., Malaplate, J., March, K., 2015. New insights into the chemical structure of Y2Ti2O7−δ nanoparticles in oxide dispersion-strengthened steels designed for sodium fast reactors by electron energy-loss spectroscopy. Journal of Nuclear Materials 456, 292–301. http://dx.doi.org/10.1016/j.jnucmat.2014.09.058

Bai, Y., Yang, Y., Wang, D., Zhang, M., 2017. Influence mechanism of parameters process and mechanical properties evolution mechanism of maraging steel 300 by selective laser melting. Materials Science and Engineering: A 703, 116–123. https://doi.org/10.1016/j.msea.2017.06.033

Boegelein, T., Dryepondt, S.N., Pandey, A., Dawson, K., Tatlock, G.J., 2015. Mechanical response and deformation mechanisms of ferritic oxide dispersion strengthened steel structures produced by selective laser melting. Acta Materialia 87, 201–215. https://doi.org/10.1016/j.actamat.2014.12.047

Boegelein, T., Louvis, E., Dawson, K., Tatlock, G.J., Jones, A.R., 2016. Characterisation of a complex thin walled structure fabricated by selective laser melting using a ferritic oxide dispersion strengthened steel. Materials Characterization 112, 30–40. https://doi.org/10.1016/j.matchar.2015.11.021

Boisselier, D., Sankaré, S., 2012. Influence of Powder Characteristics in Laser Direct Metal Deposition of SS316L for Metallic Parts Manufacturing. Physics Procedia, Laser Assisted Net shape Engineering 7 (LANE 2012) 39, 455–463. https://doi.org/10.1016/j.phpro.2012.10.061

Boutard, J., Badjeck, V., Barguet, L., Barouh, C., Bhattacharya, A., Colignon, Y., Hatzoglou, C., Loyer-Prost, M., Rouffie, A., Sallez, N., Salmon-Legagneur, H., Schuler, T., 2014. Oxide dispersion strengthened ferritic steels: a basic research joint program in France. Journal of Nuclear Materials 455, 605–611. https://doi.org/10.1016/j.jnucmat.2014.08.059

Charles, J., Mithieux, J.-D., Santacreu, P.-O., Peguet, L., 2009. The ferritic stainless family: the appropriate answer to nickel volatility? Revue de Métallurgie – International Journal of Metallurgy 106, 124–139. https://doi.org/10.1051/metal/2009024

Dawson, H., Serrano, M., Cater, S., Iqbal, N., Almásy, L., Tian, Q., Jimenez-Melero, E., 2017. Impact of friction stir welding on the microstructure of ODS steel. Journal of Nuclear Materials 486, 129–137. https://doi.org/10.1016/j.jnucmat.2016.12.033

[19]

DebRoy, T., Wei, H.L., Zuback, J.S., Mukherjee, T., Elmer, J.W., Milewski, J.O., Beese, A.M., Wilson-Heid, A., De, A., Zhang, W., 2018. Additive manufacturing of metallic components – Process, structure and properties. Progress in Materials Science 92, 112–224. https://doi.org/10.1016/j.pmatsci.2017.10.001

DebRoy, T., Zuback, J., 2018. The Hardness of Additively Manufactured Alloys. https://doi.org/10.20944/preprints201810.0096.v1

Dongsheng, C., Kimura, A., Chonghong, Z., Wentuo, H., 2016. Effects of Alloying Elements on Thermal Aging Embrittlement of 15Cr Ferritic Alloys, in: Marquis, F. (Ed.), Proceedings of the 8th Pacific Rim International Congress on Advanced Materials and Processing. Springer International Publishing, pp. 529–535.

Dumont, M., Commin, L., Morfin, I., DeGeuser, F., Legendre, F., Maugis, P., 2014. Chemical composition of nano-phases studied by anomalous small-angle X-ray scattering: Application to oxide nano-particles in ODS steels. Materials Characterization 87, 138–142. https://doi.org/10.1016/j.matchar.2013.11.008

Fayazfar, H., Salarian, M., Rogalsky, A., Sarker, D., Russo, P., Paserin, V., Toyserkani, E., 2018. A critical review of powder-based additive manufacturing of ferrous alloys: Process parameters, microstructure and mechanical properties. Materials & Design 144, 98–128. https://doi.org/10.1016/j.matdes.2018.02.018

García-Junceda, A., Hernández-Mayoral, M., Serrano, M., 2012. Influence of the microstructure on the tensile and impact properties of a 14Cr ODS steel bar. Materials Science and Engineering: A 556, 696–703. https://doi.org/10.1016/j.msea.2012.07.051

Gibson, I., Rosen, D., Stucker, B., 2015. Additive Manufacturing Technologies: 3D Printing, Rapid Prototyping, and Direct Digital Manufacturing, 2nd ed. Springer-Verlag, New York.

Hengsbach, F., Koppa, P., Duschik, K., Holzweissig, M.J., Burns, M., Nellesen, J., Tillmann, W., Tröster, T., Hoyer, K.-P., Schaper, M., 2017. Duplex stainless steel fabricated by selective laser melting - Microstructural and mechanical properties. Materials & Design 133, 136–142. https://doi.org/10.1016/j.matdes.2017.07.046

Herzog, D., Seyda, V., Wycisk, E., Emmelmann, C., 2016. Additive manufacturing of metals. Acta Materialia 117, 371–392. https://doi.org/10.1016/j.actamat.2016.07.019

Hunt, R.M., Kramer, K.J., El-Dasher, B., 2015. Selective laser sintering of MA956 oxide dispersion strengthened steel. Journal of Nuclear Materials 464, 80–85. https://doi.org/10.1016/j.jnucmat.2015.04.011

King, W.E., Barth, H.D., Castillo, V.M., Gallegos, G.F., Gibbs, J.W., Hahn, D.E., Kamath, C., Rubenchik, A.M., 2014. Observation of keyhole-mode laser melting in laser powder-bed fusion additive manufacturing. Journal of Materials Processing Technology 214, 2915–2925. https://doi.org/10.1016/j.jmatprotec.2014.06.005

Kou, S., 2002. Welding Metallurgy. Wiley.

Liu, B., Wildman, R., Tuck, C., Ashcroft, I.,, Hague, R., 2011. Investigation the effect of particle size distribution on processing parameters optimization in selective laser melting process. Presented at the In proc of the Annual Int Solid Freeform Fabrication Symp. University of Texas, Austin, Texax, USA, pp. 227–238.

Miller, M.K., Kenik, E.A., Russell, K.F., Heatherly, L., Hoelzer, D.T., Maziasz, P.J., 2003. Atom probe tomography of nanoscale particles in ODS ferritic alloys. Materials Science and Engineering: A, 47 th International Field Emission Symposium 353, 140–145. https://doi.org/10.1016/S0921-5093(02)00680-9

Petch N. J., 1953. The Cleavage Strength of Polycrystals 174, 25–28.

Prashanth, K.G., Scudino, S., Chaubey, A.K., Löber, L., Wang, P., Attar, H., Schimansky, F.P., Pyczak, F., Eckert, J., 2016. Processing of Al–12Si–TNM composites by selective laser melting and evaluation of compressive and wear properties. Journal of Materials Research 31, 55–65. https://doi.org/10.1557/jmr.2015.326

Praud, M., Mompiou, F., Malaplate, J., Caillard, D., Garnier, J., Steckmeyer, A., Fournier, B., 2012. Study of the deformation mechanisms in a Fe–14% Cr ODS alloy. Journal of Nuclear Materials, Special Issue of the International Workshop on Dispersion Strengthened Steels for Advanced Nuclear Applications – DIANA 428, 90–97. https://doi.org/10.1016/j.jnucmat.2011.10.046

Sakasegawa, H., Chaffron, L., Legendre, F., Boulanger, L., Cozzika, T., Brocq, M., de Carlan, Y., 2009. Correlation between chemical composition and size of very small oxide particles in the MA957 ODS ferritic alloy. Journal of Nuclear Materials 384, 115–118. https://doi.org/10.1016/j.jnucmat.2008.11.001

Šćepanović, M., Castro, V. de, Leguey, T., Auger, M.A., Lozano-Perez, S., Pareja, R., 2016. Microstructural stability of ODS Fe–14Cr (–2W–0.3Ti) steels after simultaneous triple irradiation. Nuclear Materials and Energy 9, 490–495. https://doi.org/10.1016/j.nme.2016.08.001

Song, B., Dong, S., Deng, S., Liao, H., Coddet, C., 2014. Microstructure and tensile properties of iron parts fabricated by selective laser melting. Optics & Laser Technology 56, 451–460. https://doi.org/10.1016/j.optlastec.2013.09.017

Steckmeyer, A., 2012. Experimental study and modelling of the high temperature mechanical behaviour of oxide dispersion strengthened ferritic steels (Theses). Ecole Nationale Supérieure des Mines de Paris.

Tang, M., Pistorius, P.C., Beuth, J.L., 2017. Prediction of lack-of-fusion porosity for powder bed fusion. Additive Manufacturing 14, 39–48. https://doi.org/10.1016/j.addma.2016.12.001

Thijs, L., Verhaeghe, F., Craeghs, T., Humbeeck, J.V., Kruth, J.-P., 2010. A study of the microstructural evolution during selective laser melting of Ti–6Al–4V. Acta Materialia 58, 3303–3312. https://doi.org/10.1016/j.actamat.2010.02.004

Walker, J.C., Berggreen, K.M., Jones, A.R., Sutcliffe, C.J., 2009. Fabrication of Fe–Cr–Al Oxide Dispersion Strengthened PM2000 Alloy Using Selective Laser Melting. Adv. Eng. Mater. 11, 541–546. https://doi.org/10.1002/adem.200800407

Wasilkowska, A., Bartsch, M., Messerschmidt, U., Herzog, R., Czyrska-Filemonowicz, A., 2003. Creep mechanisms of ferritic oxide dispersion strengthened alloys. Journal of Materials Processing Technology 133, 218–224. https://doi.org/10.1016/S0924-0136(02)00237-6

Yang, Yi, Wen, Shifeng, Wei, Quisong, Li, Wei, Liu, Jie, Shi, Yusheng, 2017. Effect of scan line spacing on texture, phase and nanohardness of TiAl/TiB 2 metal matrix composites fabricated by selective laser melting. Journal of Alloys and Compounds 728, 803–814.

Yasa, E., Kruth, J.-P., 2011. Microstructural investigation of Selective Laser Melting 316L stainless steel parts exposed to laser re-melting. Procedia Engineering, 1st CIRP Conference on Surface Integrity (CSI) 19, 389–395. https://doi.org/10.1016/j.proeng.2011.11.130

Zhang, G., Zhou, Z., Mo, K., Miao, Y., Li, S., Liu, X., Wang, M., Park, J.-S., Almer, J., Stubbins, J.F., 2016. The comparison of microstructures and mechanical properties between 14Cr-Al and 14Cr-Ti ferritic ODS alloys. Materials & Design 98, 61–67. https://doi.org/10.1016/j.matdes.2016.02.117

Zhao, Q., Yu, L., Liu, Y., Huang, Y., Ma, Z., Li, H., Wu, J., 2017. Microstructure and tensile properties of a 14Cr ODS ferritic steel. Materials Science and Engineering: A 680, 347–350. https://doi.org/10.1016/j.msea.2016.10.118
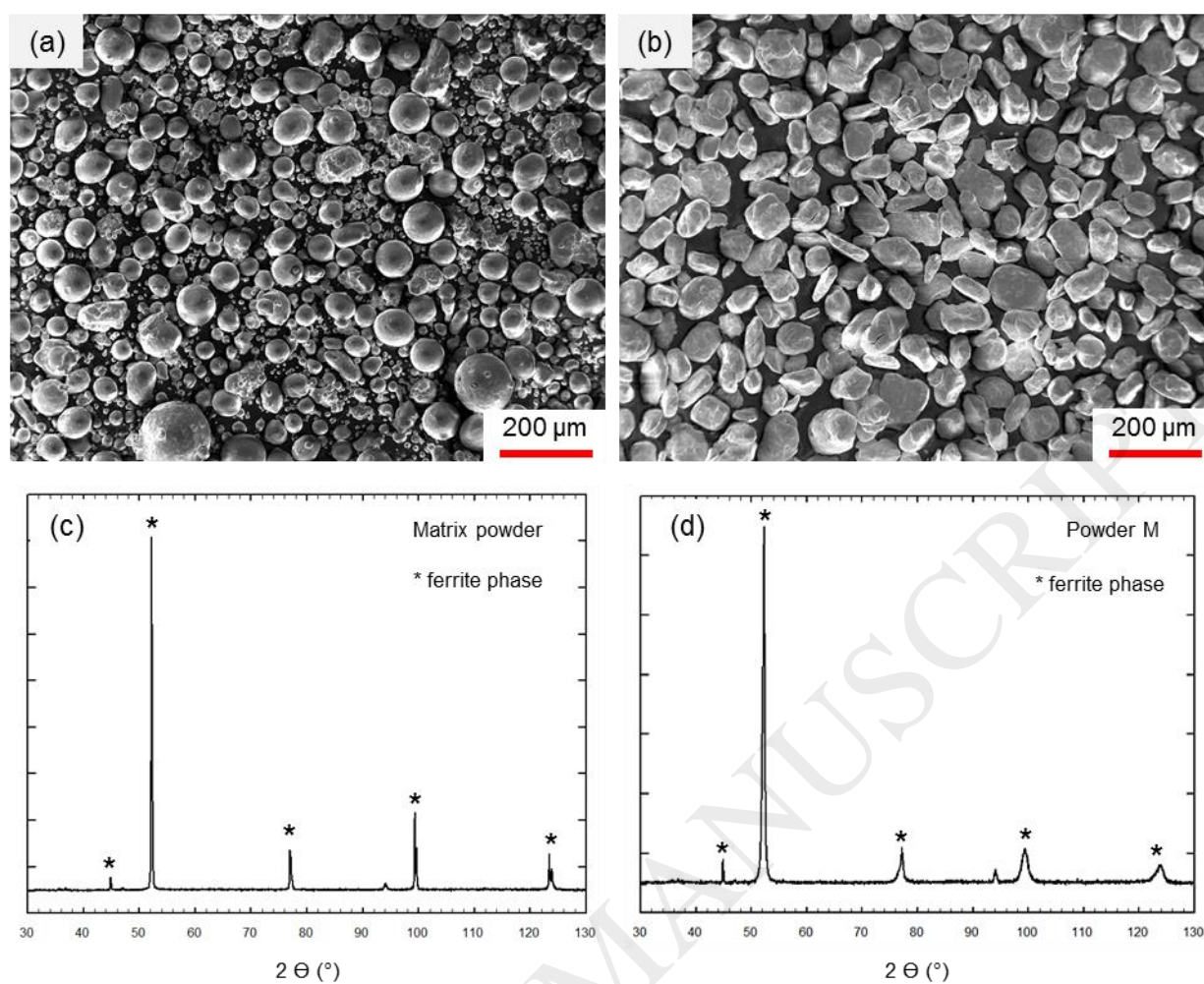
[21]

Figure 1: SEM images of (a) **the matrix material** and (b) **the powder M and**

[22]

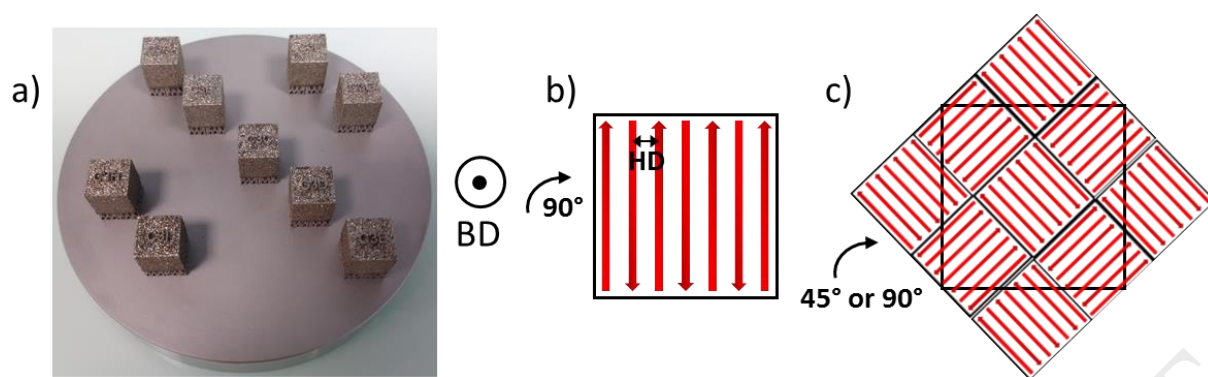*Figure 2: Picture of (a) samples connected to the substrate plate and (b) schematic of scanning strategy using parallel lines rotated of 90° between each layer and (c) using 4x4 mm island scanning pattern rotating of 45 or 90° between each layer (BD: building direction, HD: hatch distance)*
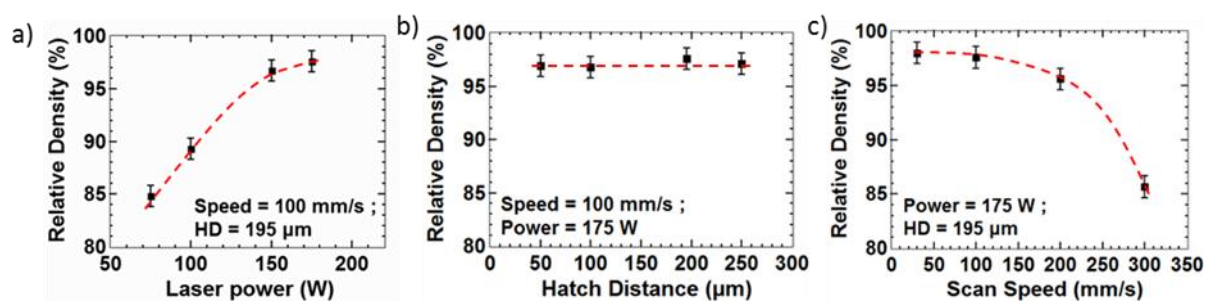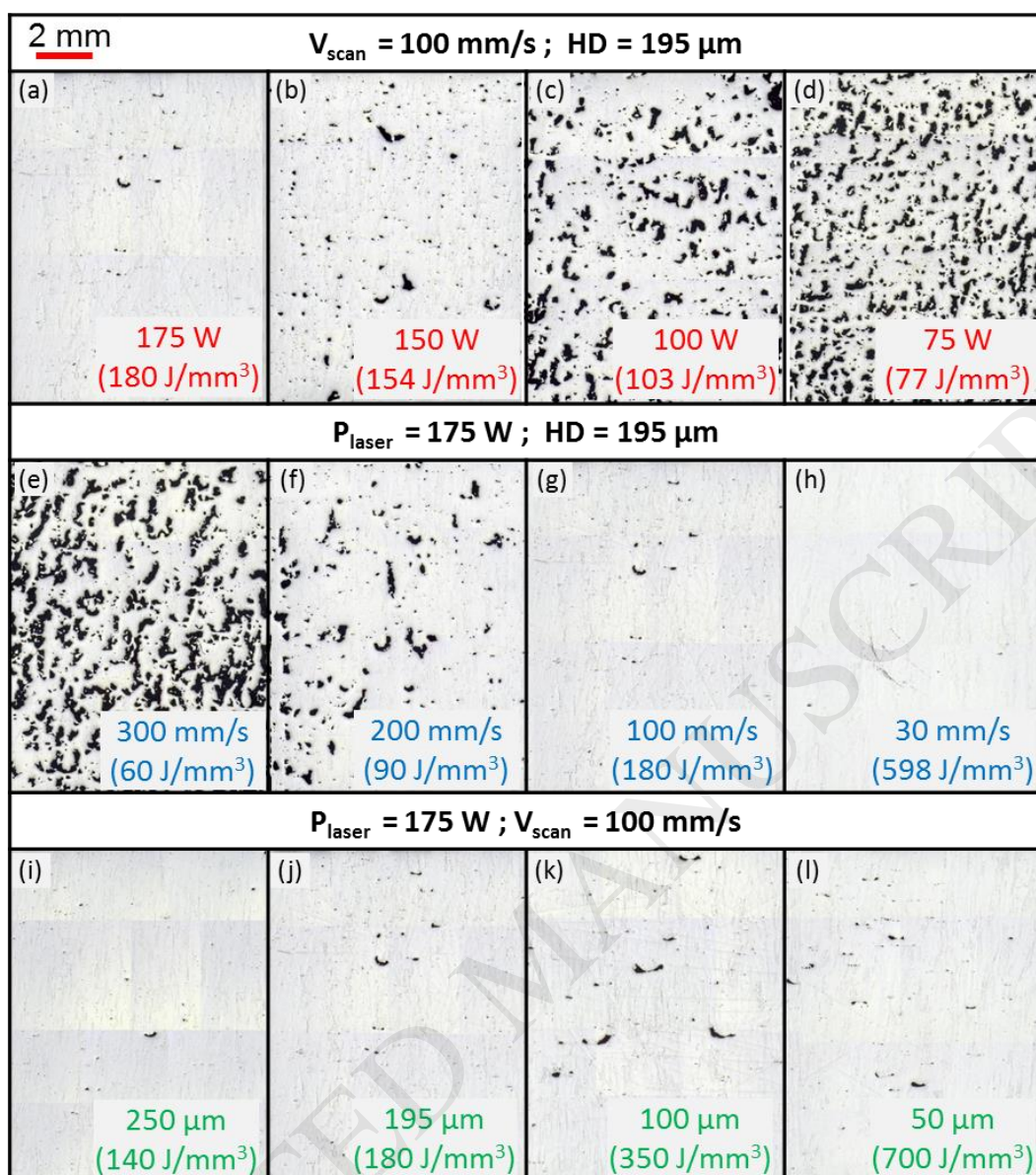
[23]

Figure 3: Effect of a) laser power; b) hatch distance and c) scan speed on the density of as-grown SLM builds

Figure 4: Optical images of the side view of SLM builds showing the effect of processing parameters on the porosities distribution: (a,b,c,d) 100 mm.s⁻¹, 195 μm and 175, 150, 100 and 75 W respectively; (e,f,g,h) 175 W, 195 μm and 300, 200, 100 and 30 mm.s⁻¹ respectively; (i,j,k,l) 175 W, 100 mm.s⁻¹ and 250, 195, 100 and 50 μm respectively. Numbers in parentheses refer to the energy densities.
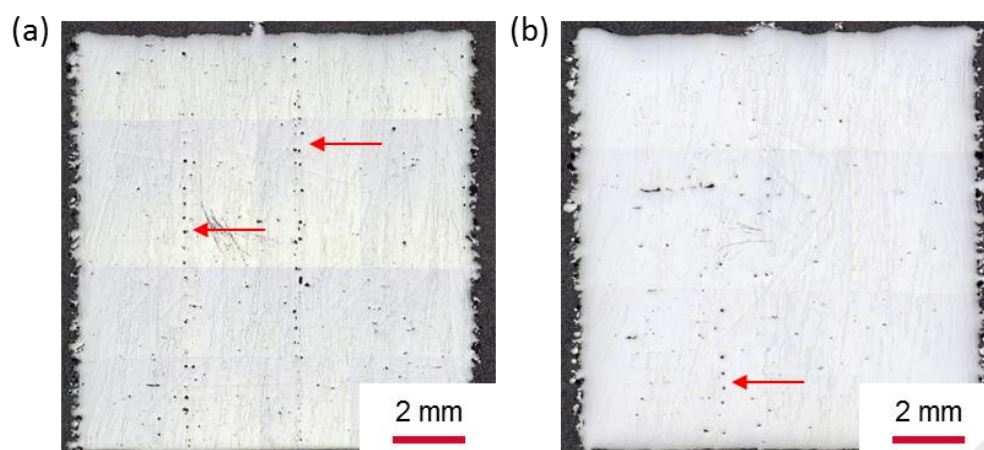
Figure 5: Optical images of porosities left between different islands when an island scanning strategy

is used with (a) a hatch distance of 195 μm and (b) a hatch distance of 100 μm

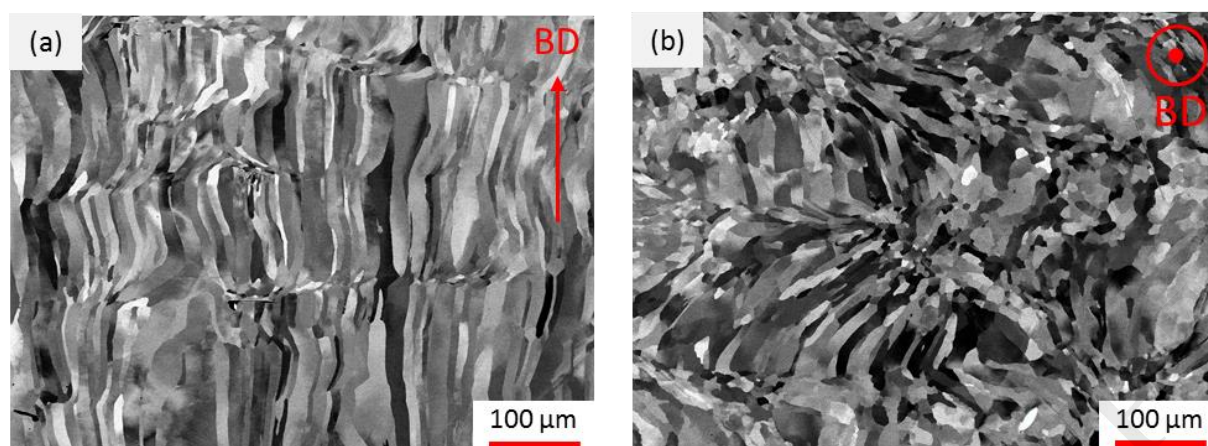P_{laser} : 175 W, V_{scan} : 100 mm/s, HD : 195 µm

Figure 6: SEM cross-section images of the microstructure of SLM builds with a laser power of 175 W, a scan speed of 100 mm.s^{-1} and a hatch distance of 195 µm viewed in two different orientations (BD: Building direction)
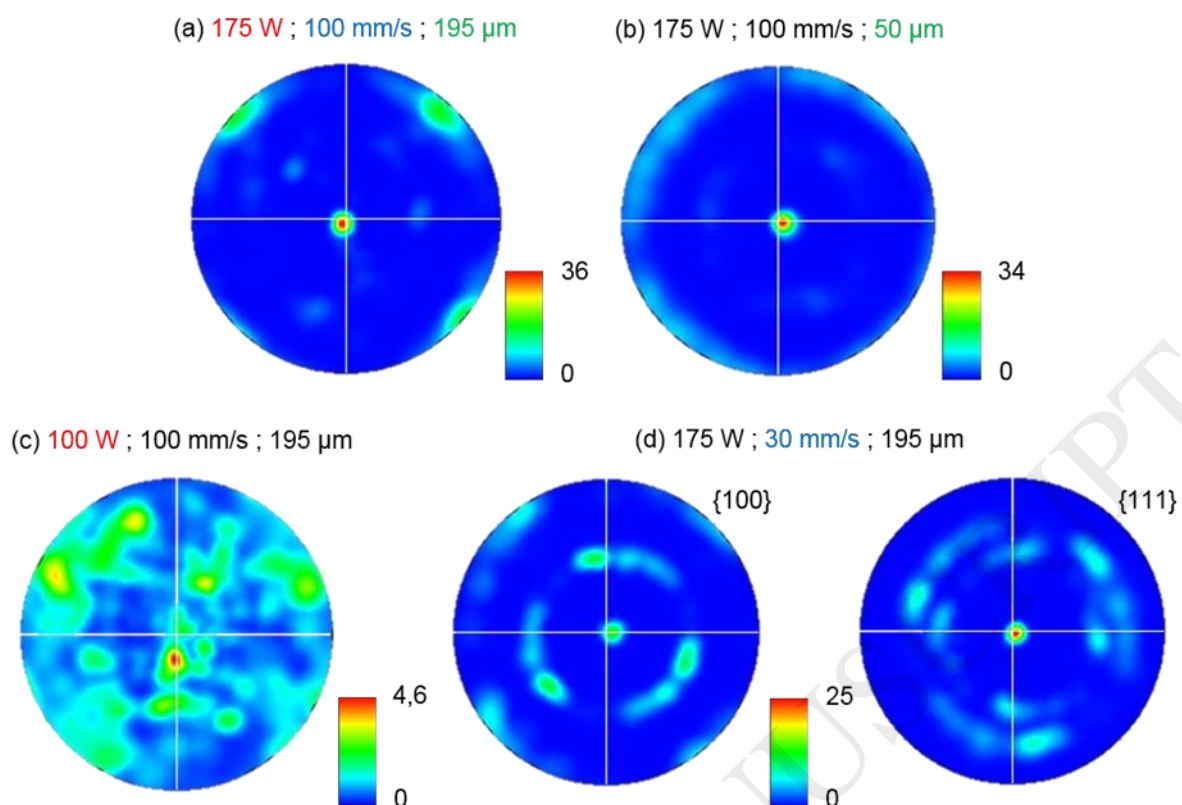
[27]

Figure 7: {100} pole figures of as-grown SLM builds at various processing parameters (the growth direction is at the center of the pole figure): a) 175 W, 100 mm.s⁻¹, 195 µm; b) 175 W, 100 mm.s⁻¹, 50 µm; c) 100 W, 100 mm.s⁻¹, 195 µm; and d) 175 W, 30 mm.s⁻¹, 195 µm.
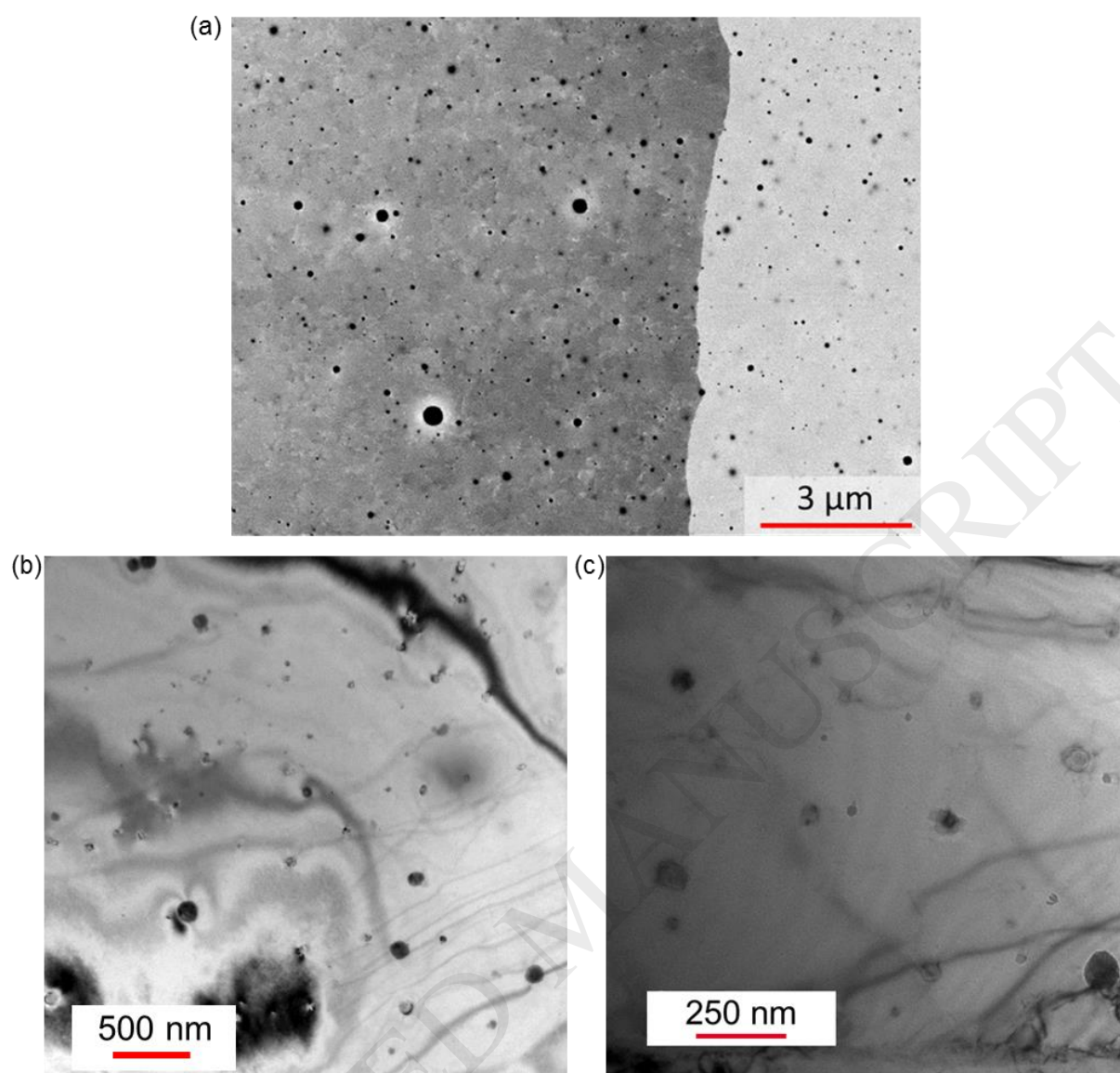
Figure 8: (a) SEM and (b) TEM images of the precipitation inside SLM builds
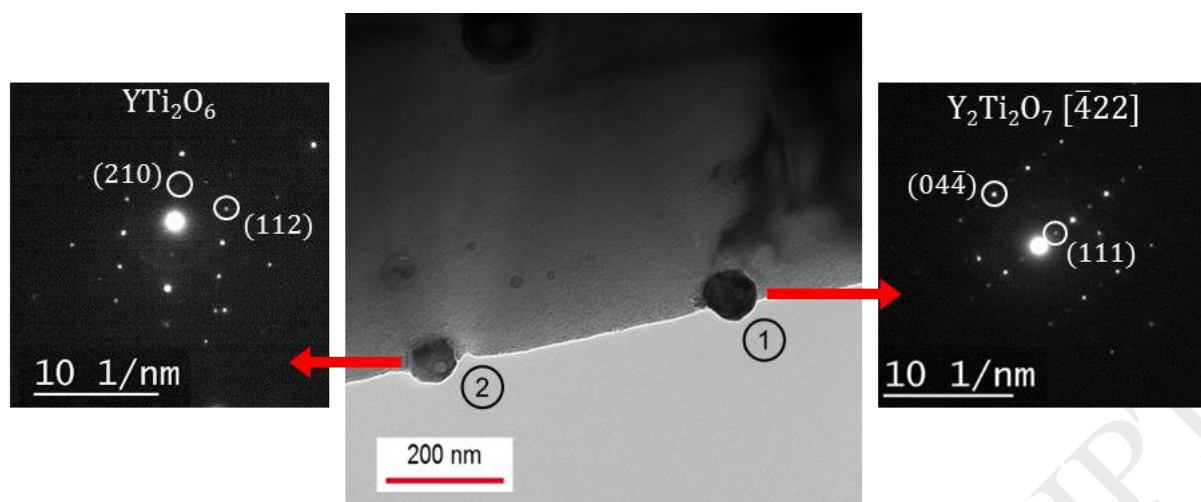
Figure 9: TEM *image and diffraction patterns of oxide particles, which are identified as $Y_2Ti_2O_7$*

(precipitate 1) and YTi_2O_6 (precipitate 2).

*Table 1 : Elemental composition (wt. %) of the powder **M** measured by ICP-OES*

Fe	Cr	W	Y	Ti	Mn	Ni
balance	14.4 ± 0.4	0.95 ± 0.03	0.31 ± 0.01	0.28 ± 0.01	0.24 ± 0.01	0.17 ± 0.01

[31]

Table 2 : Processing parameters for SLM process

Parameters	Range
Laser power	75 – **175** W
Scan speed	30 – 300 mm.s^{-1}
Hatch distance	50 – 250 µm
Layer thickness	50 µm

Table 2 : Processing parameters for SLM process

[32]

*Table 3: Grain sizes obtained by analyzing cross-sectional optical micrographs **and Vickers microhardness** of SLM builds for **various** processing parameters*

P_{laser} (W)	V_{scan} (mm.s^{-1})	HD (µm)	Relative density (%)	Grain width (µm)	Grain length (µm)	Vickers Hardness (HV)	
						Along BD	**Across BD**
175	**100**	**195**	97.5	31 ± 3	495 ± 60	189 ± 1	**178 ± 2**
100	100	195	89.3	27 ± 2	226 ± 32	175 ± 3	**169 ± 4**
175	**300**	195	85.7	26 ± 3	336 ± 60	170 ± 3	**171 ± 5**
175	100	**50**	96.9	43 ± 4	411 ± 47	173 ± 1	**159 ± 3**
Extruded ODS steel (García-Junceda et al., 2012)			100	0.1 to 3	3 to 9	**362 ± 6**	**392 ± 4**